CEAS Aeronaut J (2013) 4:175–189
DOI 10.1007/s13272-013-0063-2

ORIGINAL PAPER

A refined structural model for static aeroelastic response and divergence of metallic and composite wings

Erasmo Carrera · Alberto Varello · Luciano Demasi

Received: 30 January 2012 / Revised: 24 May 2012 / Accepted: 28 January 2013 / Published online: 27 February 2013

Abstract A refined beam model with hierarchical features is in this work extended to the static aeroelastic analysis of lifting surfaces made of metallic and composite materials. The refined structural one-dimensional (1D) theory is based on the Carrera Unified Formulation and it permits to take into account any cross-section deformation, including warping effects. The vortex lattice method is employed to provide aerodynamic loadings along the two in-plane wing directions (wing span and wing cross-section). Applications are obtained by developing a coupled aeroelastic computational model which is based on the finite element method. The accuracy of the proposed 1D model is shown by a number of applications related to various wings made of metallic and composite materials. The effect of the cross-section deformation is evaluated on the aeroelastic static response and divergence of the considered wings. The need of higher-order expansions is underlined as well as the limitations of beam results which are based on classical theories. Comparison with results obtained by existing plate/shell aeroelastic models shows that the present 1D model could result less expensive from the computational point of view with respect to shell cases. The beneficial effects of aeroelastic tailoring in the case of wings made of composite anisotropic materials are also confirmed by the present analysis.

Keywords Finite element analysis · Aeroelasticity · Higher-order 1D elements · Unified formulation

E. Carrera · A. Varello (✉)
Politecnico di Torino, Department of Mechanical and Aerospace Engineering, Corso Duca degli Abruzzi 24, 10129 Torino, Italy
e-mail: alberto.varello@polito.it

E. Carrera
e-mail: erasmo.carrera@polito.it

L. Demasi
Department of Aerospace Engineering,
San Diego State University, San Diego,
CA 92182-1308, USA
e-mail: ldemasi@mail.sdsu.edu

1 Introduction

Composite materials are widely used nowadays in a large variety of applications and engineering fields. The advantages related to their spread are becoming so significant that composites are by now a must for state-of-the-art manufacturing technology. The requirements of weight saving and structural efficiency for aerospace systems such as aircraft wings, helicopter rotor blades, and turbine blades are leading to a wide use of structures in the form of composite thin-walled beams. Furthermore, the forthcoming employment of composite materials in next-generation aircraft configurations will be certainly valuable, on the strength of the last few years design studies. Among the possible future applications, high-altitude long-endurance aircraft (HALE) [1], strut-braced wings [2], truss-braced wings [3], and C-wing configurations [4] are worth mentioning.

With the advent of composites, the accurate evaluation of the response of deformable lifting bodies (LBs) when subjected to steady and unsteady aerodynamic loadings is an even more challenging issue for the aeroelastic design of aerospace vehicles [5]. The successful construction of the Grumman X-29 forward-swept wing experimental aircraft was the best example of the exceptional interest afforded to this issue [6]. In last decades, a considerable amount of research activity devoted to the aeroelastic analysis and optimization was undertaken since the idea of aeroelastic tailoring to avoid divergence instability of forward-swept

wing was suggested many years ago [7]. Valuable contributions have been made by Weisshaar [8, 9] who considered aeroelastic problems of forward-swept wings including spanwise lift redistribution and aileron effectiveness. A discussion on the various techniques adopted in the literature to introduce a bending-twist coupling parameter to be used in tailoring was also carried out by the same author [10]. Housner and Stein [11] investigated the flutter characteristic of box-beam structures with cross-ply symmetrically laminated skins and variable stiffness properties. This parametric study included the effect of filament orientation upon the flutter speed for wings with various sweep, mass ratios, and skin thickness. A thin-walled anisotropic beam model incorporating non-classical effects was introduced by Librescu and Song [12] to analyze the sub-critical static aeroelastic response and the divergence instability of swept-forward wing structures. A review was carried out by Patil [13], who investigated the variation of aeroelastic critical speeds with composite ply lay-up of box beams via the unsteady Theodorsen's theory. The 2D cross-section was structurally modeled using an asymptotically correct cross-sectional analysis. Qin and Librescu [14] developed an aeroelastic model to investigate the influence of directionally property of composite materials and non-classical effects such as transverse shear and warping restraint on the aeroelastic instability of thin-walled aircraft wings featuring circumferentially asymmetric stiffness lay-up. Among the several composite rotor blades applications, the work done by Jeon et al. [15, 16] concerning the steady equilibrium deflections and aeroelastic modal damping via a large deflection type beam theory with small strains is worth mentioning. A recent investigation on the minimum weight design of composite plate wings subjected to the constraints on flutter and divergence speeds has been conducted by Kameyama and Fukunaga [17] using a genetic algorithm and a finite element approach. An interesting aeroelastic design optimization of a slender, thin-walled, isotropic unswept wing against divergence has been carried out by Librescu and Maalawi [18].

Detailed structural and aeroelastic models are essential to fully exploit non-classical effects in design of composite beam-like structures due to the properties characterizing advanced composite materials, such as anisotropy, heterogeneity, transverse shear flexibility [19, 20] and torsional warping [21]. As well as the accuracy, the computational cost of a refined model becomes also important especially for aeroelastic analysis where the fluid-structure coupling is addressed. Beam-like components can be analyzed by means of one-dimensional formulations and one main advantage is that 1D models require a lower computational cost compared with 2D plate and shell or 3D solid models. A detailed review of the recent development of refined beam models can be found in [22]. A considerable amount of work was done in trying to improve the global response of classical beam theories [23, 24] using appropriate shear correction factors, as described by Timoshenko [24]. El Fatmi [25, 26] improved the displacement field over the beam cross-section by introducing a warping function to refine the description of normal and shear stress of the beam. Generalized beam theories (GBT) originated with Schardt's work [27] and improved classical theories using a piecewise beam description of thin-walled sections [28, 29]. An asymptotic type expansion in conjunction with variational methods was proposed by Berdichevsky et al. [30], where a commendable review of prior works on beam theory development was given. An alternative approach in formulating refined beam theories based on asymptotic variational methods (VABS) has led to an extensive contribution in last decade by Volovoi, Hodges, Popescu [31, 32], Yu and co-workers [33, 34].

Carrera and co-authors have recently proposed refined 1D theories with only generalized displacement variables for the analysis of compact and thin-walled sections/airfoils with a remarkable reduction in the computational cost required. Higher-order models are obtained in the framework of the Carrera Unified Formulation (CUF). This formulation has been developed over the last decade for plate/shell models [35] and has recently been extended to beam static and dynamic modeling [36–39]. CUF is a hierarchical formulation which considers the order of the model as a free-parameter (i.e. an input) of the analysis. In other words, refined models are obtained with no need for ad hoc formulations. Beam theories are obtained on the basis of Taylor-type expansions. Euler–Bernoulli and Timoshenko beam theories are obtained as particular cases of the first-order expansion. The finite element method is used to handle arbitrary geometries as well as geometrical and loading conditions.

The present work couples a refined one-dimensional model based on CUF to the vortex lattice method (VLM) for the static aeroelastic analysis (SAA) of composite aircraft wings. The CUF–VLM coupling has been introduced in [40] to analyze the structural response of isotropic aircraft wings. The aeroelastic extension is here formulated to compute the aeroelastic stiffness matrix and compare the structural and aeroelastic behavior of composite beam-like wings. The computation of linear steady aerodynamic loads refers to the VLM presented by Katz and Plotkin [41]. The aerodynamic load transfer is based on the work presented by Demasi and Livne [5] via the infinite plate spline (IPS) method introduced by Harder et al. [42, 43]. The aeroelastic formulation refers to the preliminary work done by Varello et al. [44] on isotropic flat plates, now focusing on the instability divergence detection and the effect of

composite material lay-up on the aeroelastic response of moderate and high-aspect ratio wing configurations.

2 Preliminaries

A beam is a structure whose axial length L is predominant with respect to the other two orthogonal dimensions. The intersection of the beam with a plane that is perpendicular to its axis identifies the so-called beam's cross-section Ω. As shown in Fig. 1, a local cartesian coordinate system composed of x and z axes parallel to the cross-section plane is defined, whereas y represents the out-of-plane coordinate. However, the y axis is not necessarily a centroidal one.

For instance, in the case of an arbitrarily oriented beam, the local y axis might not be the beam geometrical axis. This gives high versatility to the present structural beam model. u_x, u_y, and u_z are the cartesian components of the displacement vector:

$$\boldsymbol{u}(x,y,z) = \{u_x \quad u_y \quad u_z\}^{\mathrm{T}} \tag{1}$$

where superscript T stands for the transposition operator. The stress, $\boldsymbol{\sigma}$, and the strain, $\boldsymbol{\varepsilon}$, are grouped in vectors as follows:

$$\begin{aligned} \boldsymbol{\sigma}_p &= \{\sigma_{zz} \quad \sigma_{xx} \quad \sigma_{zx}\}^{\mathrm{T}} \quad \boldsymbol{\varepsilon}_p = \{\varepsilon_{zz} \quad \varepsilon_{xx} \quad \varepsilon_{zx}\}^{\mathrm{T}} \\ \boldsymbol{\sigma}_n &= \{\sigma_{zy} \quad \sigma_{xy} \quad \sigma_{yy}\}^{\mathrm{T}} \quad \boldsymbol{\varepsilon}_n = \{\varepsilon_{zy} \quad \varepsilon_{xy} \quad \varepsilon_{yy}\}^{\mathrm{T}} \end{aligned} \tag{2}$$

Subscript p refers to quantities related to the beam cross-section Ω, whereas subscript n refers to quantities related to the out-of-plane direction. In the case of small displacements with respect to the length L, the linear relations between strain and displacement components hold and a compact vectorial notation can be adopted:

$$\begin{aligned} \boldsymbol{\varepsilon}_p &= \boldsymbol{D}_p \boldsymbol{u} \\ \boldsymbol{\varepsilon}_n &= \boldsymbol{D}_n \boldsymbol{u} = \boldsymbol{D}_{np}\boldsymbol{u} + \boldsymbol{D}_{ny}\boldsymbol{u} \end{aligned} \tag{3}$$

where $\boldsymbol{D}_p, \boldsymbol{D}_{np}$, and $\boldsymbol{D}_{ny}$ are differential operator matrices:

$$\begin{aligned} \boldsymbol{D}_p &= \begin{bmatrix} 0 & 0 & \frac{\partial}{\partial z} \\ \frac{\partial}{\partial x} & 0 & 0 \\ \frac{\partial}{\partial z} & 0 & \frac{\partial}{\partial x} \end{bmatrix}, \boldsymbol{D}_{np} = \begin{bmatrix} 0 & \frac{\partial}{\partial z} & 0 \\ 0 & \frac{\partial}{\partial x} & 0 \\ 0 & 0 & 0 \end{bmatrix}, \\ \boldsymbol{D}_{ny} &= \begin{bmatrix} 0 & 0 & \frac{\partial}{\partial y} \\ \frac{\partial}{\partial y} & 0 & 0 \\ 0 & \frac{\partial}{\partial y} & 0 \end{bmatrix} \end{aligned} \tag{4}$$

According to Eq. 2, in the case of beams made of linear elastic orthotropic materials, the generalized Hooke's law holds:

$$\begin{aligned} \boldsymbol{\sigma}_p &= \widetilde{\boldsymbol{C}}_{pp}\boldsymbol{\varepsilon}_p + \widetilde{\boldsymbol{C}}_{pn}\boldsymbol{\varepsilon}_n \\ \boldsymbol{\sigma}_n &= \widetilde{\boldsymbol{C}}_{np}\boldsymbol{\varepsilon}_p + \widetilde{\boldsymbol{C}}_{nn}\boldsymbol{\varepsilon}_n \end{aligned} \tag{5}$$

where matrices $\widetilde{\boldsymbol{C}}_{pp}$, $\widetilde{\boldsymbol{C}}_{pn}$, $\widetilde{\boldsymbol{C}}_{np}$ and $\widetilde{\boldsymbol{C}}_{nn}$ are:

$$\begin{aligned} \widetilde{\boldsymbol{C}}_{pp} &= \begin{bmatrix} \widetilde{C}_{11} & \widetilde{C}_{12} & 0 \\ \widetilde{C}_{12} & \widetilde{C}_{22} & 0 \\ 0 & 0 & \widetilde{C}_{44} \end{bmatrix}, \\ \widetilde{\boldsymbol{C}}_{pn} &= \widetilde{\boldsymbol{C}}_{np}^{T} = \begin{bmatrix} 0 & \widetilde{C}_{16} & \widetilde{C}_{13} \\ 0 & \widetilde{C}_{26} & \widetilde{C}_{23} \\ \widetilde{C}_{45} & 0 & 0 \end{bmatrix}, \\ \widetilde{\boldsymbol{C}}_{nn} &= \begin{bmatrix} \widetilde{C}_{55} & 0 & 0 \\ 0 & \widetilde{C}_{66} & \widetilde{C}_{36} \\ 0 & \widetilde{C}_{36} & \widetilde{C}_{33} \end{bmatrix} \end{aligned} \tag{6}$$

For the sake of brevity, the dependence of the coefficients $\widetilde{C}_{ij}$ on Young's moduli, Poisson's ratios, shear moduli and the fiber orientation angle θ is not reported here. It can be found in Jones [45].

3 Refined beam theory

According to the framework of CUF [35], the displacement field is assumed to be an expansion of a certain class of functions F_τ, which depend on the cross-section coordinates x and z:

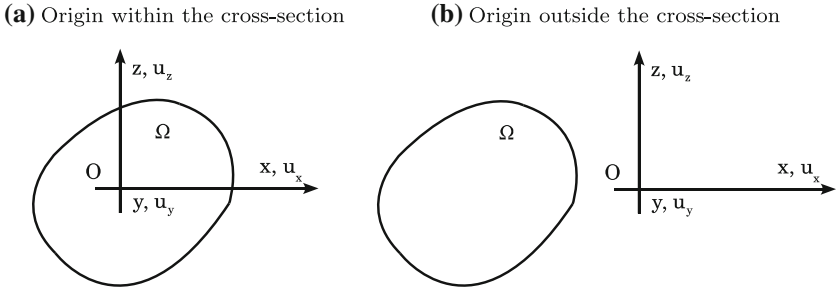

Fig. 1 Beam's cross-section geometry and coordinate system

$$\boldsymbol{u}(x,y,z) = F_\tau(x,z)\boldsymbol{u}_\tau(y) \quad \tau = 1,\ 2,\ \ldots,\ M = M(N) \tag{7}$$

The compact expression is based on Einstein's notation: repeated subscript τ indicates summation. The number of expansion terms M depends on the expansion order N, which is a free parameter of the formulation. Multivariate Maclaurin's polynomials of the x and z variables are chosen as cross-section functions F_τ.

Most displacement-based theories can be formulated on the basis of the above generic kinematic field. For instance, when $N = 2$, the second-order axiomatic displacement field is given by:

$$\begin{aligned} u_x &= u_{x1} + u_{x2}x + u_{x3}z + u_{x4}x^2 + u_{x5}xz + u_{x6}z^2 \\ u_y &= u_{y1} + u_{y2}x + u_{y3}z + u_{y4}x^2 + u_{y5}xz + u_{y6}z^2 \\ u_z &= u_{z1} + u_{z2}x + u_{z3}z + u_{z4}x^2 + u_{z5}xz + u_{z6}z^2 \end{aligned} \tag{8}$$

Subsequently, the classical beam models such as Timoshenko's (TBM) [24] and Euler–Bernoulli's (EBBM) [23] are easily derived from the first-order approximation model ($N = 1$). TBM can be obtained by setting terms $\{u_{ij}\colon i = x,\ z;\ j = 2\ ,\ 3\}$ equal to zero:

$$\begin{aligned} u_x &= u_{x1} \\ u_y &= u_{y1} + u_{y2}x + u_{y3}z \\ u_z &= u_{z1} \end{aligned} \tag{9}$$

In addition, an infinite rigidity in the transverse shear is also adopted for EBBM by penalizating ε_{zy} and ε_{xy} via a high penalty value in the following constitutive equations:

$$\begin{aligned} \sigma_{zy} &= \widetilde{C}_{45}\,\varepsilon_{zx} + \widetilde{C}_{55}\,\varepsilon_{zy} \\ \sigma_{xy} &= \widetilde{C}_{16}\,\varepsilon_{zz} + \widetilde{C}_{26}\,\varepsilon_{xx} + \widetilde{C}_{66}\,\varepsilon_{xy} + \widetilde{C}_{36}\,\varepsilon_{yy} \end{aligned} \tag{10}$$

Higher-order models provide an accurate description of the shear mechanics, the cross-section deformation, Poisson's effect along the spatial directions and the torsional mechanics in more detail than classical models do. Traditional kinematic assumptions of EBBM neglect them all, since this model was formulated to describe the bending mechanics. TBM takes into account constant shear stress and strain components. Classical theories and the first-order model require the assumption of opportunely reduced material stiffness coefficients to correct Poisson's locking effect [46]. According to Carrera and Giunta [37], the same technique is used here to correct Poisson's locking.

4 The FE structural stiffness matrix

Following standard FEM, the unknown variables in the element domain are expressed in terms of their values corresponding to the element nodes [38]. By introducing the shape functions N_i and the nodal displacement vector $\boldsymbol{q}$, the displacement field becomes:

$$\boldsymbol{u}(x,y,z) = F_\tau(x,z)N_i(y)\boldsymbol{q}_{\tau i} \quad i = 1,\ 2,\ \ldots,\ M_N \tag{11}$$

where:

$$\boldsymbol{q}_{\tau i} = \{q_{u_{x\tau i}} \quad q_{u_{y\tau i}} \quad q_{u_{z\tau i}}\}^{\mathrm{T}} \tag{12}$$

contains the degrees of freedom of the τth expansion term corresponding to the ith element node. One-dimensional elements with M_N number of nodes equal to 2, 3 and 4 are formulated and named B2, B3 and B4, respectively. The results reported in the present work involve only B4 elements. Third-order Lagrange polynomials are used as shape functions [47].

As far as the number of DOFs is concerned, $N = 1$ model leads to three unknowns for each displacement component u_x, u_y, u_z and then 9 DOFs per node, whereas the fourth-order model involves 15 unknowns per displacement component and 45 DOFs per node. For the sake of brevity, more details are not reported here, but can be found in Carrera et al. [39]. This beam model can be easily extended to mixed theories. However, this work presents a displacement-based formulation. The variational statement is therefore the principle of virtual displacements:

$$\delta L_{\mathrm{int}} = \int_V \left(\delta\boldsymbol{\varepsilon}_n^{\mathrm{T}}\boldsymbol{\sigma}_n + \delta\boldsymbol{\varepsilon}_p^{\mathrm{T}}\boldsymbol{\sigma}_p\right)\mathrm{d}V = \delta L_{\mathrm{ext}} \tag{13}$$

where L_{int} is the internal strain energy and L_{ext} is the external work. δ stands for the virtual variation. Substituting Eq. 11 into Eq. 3 and using the fact that F_τ are not dependent on y, the strain vectors can be written as:

$$\begin{aligned} \boldsymbol{\varepsilon}_n &= \left(\boldsymbol{D}_{np}F_\tau\boldsymbol{I}\right)N_i\boldsymbol{q}_{\tau i} + F_\tau\left(\boldsymbol{D}_{ny}N_i\boldsymbol{I}\right)\boldsymbol{q}_{\tau i} \\ \boldsymbol{\varepsilon}_p &= \left(\boldsymbol{D}_pF_\tau\boldsymbol{I}\right)N_i\boldsymbol{q}_{\tau i} \end{aligned} \tag{14}$$

Therefore, the expression of the internal strain energy (Eq. 13) can be rewritten in terms of virtual nodal displacements as follows:

$$\delta L_{\mathrm{int}} = \delta\boldsymbol{q}_{\tau i}^{\mathrm{T}}\,\boldsymbol{K}^{ij\tau s}\,\boldsymbol{q}_{sj} \tag{15}$$

where Eq. 5 has been used. The 3×3 *fundamental nucleus* of the structural stiffness matrix presented in Eq. 15 can be shown to have the following explicit equation:

$$\begin{aligned} \boldsymbol{K}^{ij\tau s} = {} & E_{ij} \triangleleft \left(\boldsymbol{D}_{np}^{\mathrm{T}}F_\tau\boldsymbol{I}\right)\left[\widetilde{\boldsymbol{C}}_{np}\left(\boldsymbol{D}_pF_s\boldsymbol{I}\right) + \widetilde{\boldsymbol{C}}_{nn}\left(\boldsymbol{D}_{np}F_s\boldsymbol{I}\right)\right] \\ & + \left(\boldsymbol{D}_p^{\mathrm{T}}F_\tau\boldsymbol{I}\right)\left[\widetilde{\boldsymbol{C}}_{pp}\left(\boldsymbol{D}_pF_s\boldsymbol{I}\right) + \widetilde{\boldsymbol{C}}_{pn}\left(\boldsymbol{D}_{np}F_s\boldsymbol{I}\right)\right] \triangleright_\Omega \\ & + E_{ij,_y} \triangleleft \left[\left(\boldsymbol{D}_{np}^{\mathrm{T}}F_\tau\boldsymbol{I}\right)\widetilde{\boldsymbol{C}}_{nn} + \left(\boldsymbol{D}_p^{\mathrm{T}}F_\tau\boldsymbol{I}\right)\widetilde{\boldsymbol{C}}_{pn}\right]F_s \triangleright_\Omega \boldsymbol{I}_{\Omega y} \\ & + E_{i,_yj}\boldsymbol{I}_{\Omega y}^{\mathrm{T}} \triangleleft F_\tau\left[\widetilde{\boldsymbol{C}}_{np}\left(\boldsymbol{D}_pF_s\boldsymbol{I}\right) + \widetilde{\boldsymbol{C}}_{nn}\left(\boldsymbol{D}_{np}F_s\boldsymbol{I}\right)\right] \triangleright_\Omega \\ & + E_{i,_yj,_y}\boldsymbol{I}_{\Omega y}^{\mathrm{T}} \triangleleft F_\tau\widetilde{\boldsymbol{C}}_{nn}F_s \triangleright_\Omega \boldsymbol{I}_{\Omega y} \end{aligned} \tag{16}$$

where:

$$\boldsymbol{I}_{\Omega y} = \begin{bmatrix} 0 & 0 & 1 \\ 1 & 0 & 0 \\ 0 & 1 & 0 \end{bmatrix} \quad \triangleleft \cdots \triangleright_{\Omega} = \int_{\Omega} \ldots \mathrm{d}\Omega \tag{17}$$

$$\left(E_{ij}, E_{ij_{,y}}, E_{i_{,y}j}, E_{i_{,y}j_{,y}}\right) = \int_{l} \left(N_i N_j, N_i N_{j_{,y}}, N_{i_{,y}} N_j, N_{i_{,y}} N_{j_{,y}}\right) \mathrm{d}y \tag{18}$$

The integration over Ω can be performed numerically over an arbitrary cross-section and is indicated by the symbol $\triangleleft \cdots \triangleright_{\Omega}$. It should be noted that no assumptions on the expansion order have been made. Therefore, it is possible to obtain refined beam models without changing the formal expression of the nucleus components. The present model is invariant with respect to the order of the beam theory and the type of element used in the finite element axial discretization. Shear locking is corrected through selective integration via a typical reduced Gauss integration [47] of the terms in Eq. 18 related to the transverse shear. Full integration is adopted for the other terms.

The construction of the Stiffness Matrix $\boldsymbol{K}$ in Eq. 16 is formally independent of the choice of cross-section functions. Maclaurin's polynomials are here used to develop equivalent single-layer models, where a homogenization of the material properties is conducted by summing the contributions of each layer in the stiffness matrix. For laminated cross-sections, a layerwise description may be preferred in order to detect local effects of composite materials more accurately than an equivalent single-layer approach. Thus, an expansion of Lagrange polynomials may be used in Eq. 7 instead of Maclaurin's polynomials as described in [48].

5 Steady aerodynamic forces by VLM

Classical beam models provide acceptable results only for relatively high aspect ratio beams. With the proposed hierarchical beam formulation based on CUF, the accuracy of the axiomatic model can be freely increased. This implies that the present method can be used also for small aspect ratio. Therefore, it is an ideal tool to analyze large aspect ratio wings typical of HALE vehicles and even small aspect ratio wing configurations such as delta wings, see [38]. Moreover, non-planar wing configurations with arbitrary orientation in the 3D space, such as tapered wings with dihedral and sweep angles, can be successfully addressed with the proposed beam model.

The aerodynamic method here chosen is the VLM [41]. The aerodynamic mesh, which consists in a lattice of N_{AP} quadrilateral panels, lies on a reference trapezoidal surface with 2 edges parallel to the wind direction. For each panel, the aerodynamic force is applied at the load point P_L, whereas the wall tangency condition is imposed at the control point P_C. As shown in Fig. 2, a second coordinate system $x_{\mathrm{loc}'} - y_{\mathrm{loc}'} - z_{\mathrm{loc}'}$ is introduced so that the reference surface lies on the $x_{\mathrm{loc}'} - y_{\mathrm{loc}'}$ plane. A global coordinate system $x - y - z$ is placed on the airfoil's leading edge point at the wing root section so that x and $x_{\mathrm{loc}'}$ axes are both parallel to the free stream velocity $\boldsymbol{V}_{\infty}$ (see Fig. 2).

The wing is modeled with a straight beam. The structural FE mesh is contained along the y_{loc} axis, which is on the trapezoidal reference surface. The fundamental nucleus (see Eq. 16) was derived in the local coordinate system $x_{\mathrm{loc}} - y_{\mathrm{loc}} - z_{\mathrm{loc}}$. Thus, Eq. 15 is slightly modified to reflect this fact by introducing the subscript "loc" and the expression of the fundamental nucleus in the global coordinate system is obtained:

$$\begin{aligned} \delta L_{\mathrm{int}} &= \delta \boldsymbol{q}_{\tau i\,\mathrm{loc}}^{\mathrm{T}} \boldsymbol{K}_{\mathrm{loc}}^{ij\tau s} \boldsymbol{q}_{sj\,\mathrm{loc}} = \delta \boldsymbol{q}_{\tau i}^{\mathrm{T}} \left[\boldsymbol{e}^{\mathrm{T}} \cdot \boldsymbol{K}_{\mathrm{loc}}^{ij\tau s} \cdot \boldsymbol{e}\right] \boldsymbol{q}_{sj} \\ &= \delta \boldsymbol{q}_{\tau i}^{\mathrm{T}} \boldsymbol{K}^{ij\tau s} \boldsymbol{q}_{sj} \end{aligned} \tag{19}$$

where $\boldsymbol{e}$ is a 3×3 rotation matrix. The finite element assembly procedure to build $\boldsymbol{K}$ enforces the compatibility of the displacements expressed in global coordinates. The present beam model allows a very accurate calculation of the displacement field at any point of the three-dimensional wing. Based on this property, the infinite plate spline method [4, 5, 42] was shown (see [44]) to be the ideal choice for the aerodynamic loads transfer with the multi-fidelity beam model presented in this work.

The coordinate system for the splining is the local′ one. A set of N_{PS} points is chosen on the wing reference surface. The displacements of these points can be accurately calculated with the advanced beam model and are used for the splining. They are not coincident with the finite element

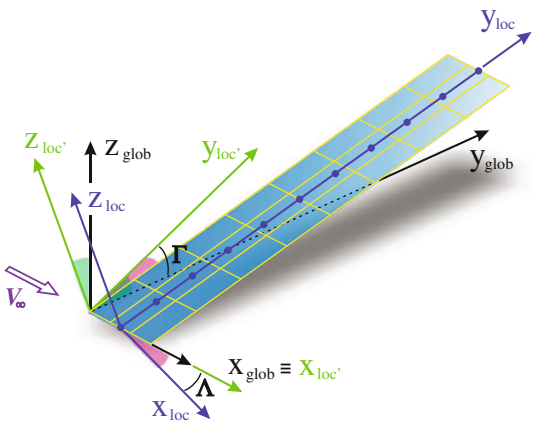

Fig. 2 One-dimensional structural mesh and two-dimensional aerodynamic mesh of the wing structure

nodes. However, they are "seen" as structural points in the splining and hence indicated as *pseudo-structural points*. The final expressions relating the transverse displacements at the aerodynamic load points and the slopes at the aerodynamic control points to the nodal DOFs vector via the splining technique are respectively:

$$\widetilde{\mathcal{Z}}_{\mathrm{loc}'} = \widetilde{\boldsymbol{A}}_3^{\bigstar} \cdot \boldsymbol{q} \tag{20}$$

$$\frac{\mathrm{d}\mathcal{Z}_{\mathrm{loc}'}}{\mathrm{dx}_{\mathrm{loc}'}} = \frac{\mathrm{d}\mathcal{Z}_{\mathrm{loc}'}}{\mathrm{dx}} = \boldsymbol{A_3} \cdot \boldsymbol{q} \tag{21}$$

where the local$'$ coordinates of the pseudo-structural points are used to compute $\widetilde{\boldsymbol{A}}_3^{\bigstar}$ and $\boldsymbol{A}_3$. For the sake of brevity, the splining procedure is not reported here. More details about the adaptation of the IPS to the CUF beam model via a set of pseudo-structural points can be found in [40, 44].

The derivation of aerodynamic loads is now faced. According to the VLM [41], the pressures acting on the wing are transferred as lift forces located on load points of the aerodynamic panels and perpendicular to the wind direction:

$$\boldsymbol{L} = \frac{1}{2}\rho_\infty V_\infty^2 \boldsymbol{I}^{\mathrm{D}} \cdot \Delta\boldsymbol{p} \tag{22}$$

where $\Delta\boldsymbol{p}$ is the vector containing the dimensionless pressure acting on all the load points, normalized with respect to the dynamic pressure. The matrix $\boldsymbol{I}^{\mathrm{D}}$ contains the panels' geometrical data [44]. The VLM allows the dimensionless normalwash, normalized with respect to V_∞, to be described as a function of the pressures acting on each aerodynamic panel:

$$\boldsymbol{w} = \boldsymbol{A}^{\mathrm{D}} \cdot \Delta\boldsymbol{p} \tag{23}$$

where $\boldsymbol{A}^{\mathrm{D}}$ is the aerodynamic influence coefficient matrix. It is calculated using the geometrical data of the aerodynamic mesh. More details can be found in [41]. Considering that the structure changes configuration when it deforms, the wall tangency condition used for the VLM is imposed at each control point by setting the dimensionless normalwash to be equal to the local slope:

$$\boldsymbol{w} = \frac{\mathrm{d}\ \mathcal{Z}_{\mathrm{loc}}}{\mathrm{dx}} \tag{24}$$

The boundary condition relates the aerodynamics and the deflection of the structure. As a result, by combining Eqs. 22–24 and 21, the vector containing the aerodynamic forces is written as a function of nodal DOFs:

$$\begin{aligned}\boldsymbol{L} &= \frac{1}{2}\rho_\infty V_\infty^2 \boldsymbol{I}^{\mathrm{D}} \cdot \left[\boldsymbol{A}^{\mathrm{D}}\right]^{-1} \cdot \boldsymbol{w} \\ &= \frac{1}{2}\rho_\infty V_\infty^2 \boldsymbol{I}^{\mathrm{D}} \cdot \left[\boldsymbol{A}^{\mathrm{D}}\right]^{-1} \cdot \boldsymbol{A}_3 \cdot \boldsymbol{q} = \frac{1}{2}\rho_\infty V_\infty^2 \overline{\boldsymbol{c}} \cdot \boldsymbol{q}\end{aligned} \tag{25}$$

where the matrix $\overline{\boldsymbol{c}}$ has been conveniently introduced.

6 The aeroelastic stiffness matrix and divergence problem

The aerodynamic forces $\boldsymbol{L}$ of Eq. 25 are applied at load points of the aerodynamic panels and are all parallel to the $z_{\mathrm{loc}'}$ axis. The transfer of these loads at the aerodynamic points to the energetically equivalent loads at structural nodes is performed via the Principle of Virtual Displacements. The work done by the aerodynamic forces (vector $\boldsymbol{L}$) applied at the load points is equated to the work done by the equivalent nodal forces (vector $\boldsymbol{L}_{\mathrm{str}}$). Using Eq. 20 it is possible to deduce:

$$\begin{aligned}\delta W = \delta\widetilde{\mathcal{Z}}_{\mathrm{loc}'}^{\mathrm{T}} \cdot \boldsymbol{L} = \left\{\widetilde{\boldsymbol{A}}_3^{\bigstar} \cdot \delta\boldsymbol{q}\right\}^{\mathrm{T}} \cdot \boldsymbol{L} = \delta\boldsymbol{q}^{\mathrm{T}} \cdot \widetilde{\boldsymbol{A}}_3^{\bigstar\mathrm{T}} \cdot \boldsymbol{L} = \delta\boldsymbol{q}^{\mathrm{T}} \cdot \boldsymbol{L}_{\mathrm{str}} \\ \Rightarrow \boldsymbol{L}_{\mathrm{str}} = \widetilde{\boldsymbol{A}}_3^{\bigstar\mathrm{T}} \cdot \boldsymbol{L}\end{aligned} \tag{26}$$

where the virtual variation of nodal degrees of freedom $\boldsymbol{q}$ is considered. Using Eq. 25, the vector of nodal forces energetically equivalent to the aerodynamic loads can be written as:

$$\boldsymbol{L}_{\mathrm{str}} = \widetilde{\boldsymbol{A}}_3^{\bigstar^{\mathrm{T}}} \cdot \boldsymbol{L} = \frac{1}{2}\rho_\infty V_\infty^2 \widetilde{\boldsymbol{A}}_3^{\bigstar^{\mathrm{T}}} \cdot \overline{\boldsymbol{c}} \cdot \boldsymbol{q} = -\boldsymbol{K}_{\mathrm{aero}} \cdot \boldsymbol{q} \tag{27}$$

where the negative sign is adopted for the sake of convenience. Such a term can go to the left hand side of the aeroelastic equation system and $\boldsymbol{K}_{\mathrm{aero}}$ is summed up to the structural stiffness matrix:

$$\boldsymbol{K}_{\mathrm{str}} \cdot \boldsymbol{q} = \boldsymbol{L}_{\mathrm{str}} = -\boldsymbol{K}_{\mathrm{aero}} \cdot \boldsymbol{q} \tag{28}$$

$$\left[\boldsymbol{K}_{\mathrm{str}} + \boldsymbol{K}_{\mathrm{aero}}\right] \cdot \boldsymbol{q} = \boldsymbol{0} \quad \boldsymbol{K}_{\mathrm{aeroelastic}} \cdot \boldsymbol{q} = \boldsymbol{0} \tag{29}$$

where $\boldsymbol{K}_{\mathrm{aeroelastic}}$ is the *aeroelastic stiffness matrix* which couples structural and aerodynamic contributions. The stiffness of the system now takes into account the aerodynamic loads due to the deformed configuration.

Since no angle of attack has been considered so far, it seems that there is no motion from Eq. 29. So a different from zero angle of attack is now assigned to the undeformed wing and the corresponding aerodynamic lift forces acting on the panels are computed.

The wall tangency condition is now imposed at the control point of each panel by setting the dimensionless normalwash to be equal to the local slope:

$$w = \tan\left(\pi - \alpha\right) \tag{30}$$

where the angle of attack α is a small quantity (linear aerodynamic model). Following the same procedure used to build $\boldsymbol{L}_{\mathrm{str}}$, the energetically equivalent nodal loads $\boldsymbol{L}_{\mathrm{RHS}}$ (the subscript RHS means right hand side) are:

$$\boldsymbol{L}_{\mathrm{RHS}} = \frac{1}{2}\rho_\infty V_\infty^2 \tan\left(\pi - \alpha\right) \widetilde{\boldsymbol{A}}_3^{\bigstar^{\mathrm{T}}} \cdot \boldsymbol{I}^{\mathrm{D}} \left[\boldsymbol{A}^{\mathrm{D}}\right]^{-1} \boldsymbol{d} \tag{31}$$

where $\boldsymbol{d}$ stands for a $N_{AP} \times 1$ vector of ones. More details about this procedure can be found in [40]. In conclusion, the final aeroelastic equation to be solved is:

$$\boldsymbol{K}_{\text{aeroelastic}} \cdot \boldsymbol{q} = \boldsymbol{L}_{\text{RHS}} \tag{32}$$

Equation 32 allows nodal displacement vector $\boldsymbol{q}$ to be computed. It is noteworthy that $\boldsymbol{L}_{\text{RHS}}$ contains the equivalent nodal aerodynamic loads applied on the undeformed configuration upon exposure to the flow field with a different from zero angle of attack. Now that the right hand side is different from zero, we have a solution.

As far as the divergence instability is concerned, Eq. 28 is retrieved and the parameter λ depending on the free stream velocity is extracted:

$$\boldsymbol{K}_{\text{str}} \cdot \boldsymbol{q} = \boldsymbol{L}_{\text{str}} = \frac{1}{2}\rho_\infty V_\infty^2 \widetilde{\boldsymbol{A}}_3^{\star\text{T}} \cdot \overline{\boldsymbol{c}} \cdot \boldsymbol{q} = \lambda \boldsymbol{K}_{\text{aero}}^{\star} \cdot \boldsymbol{q} \tag{33}$$

where:

$$\lambda = \frac{1}{2}\rho_\infty V_\infty^2 \qquad \boldsymbol{K}_{\text{aero}}^{\star} = \widetilde{\boldsymbol{A}}_3^{\star\text{T}} \cdot \overline{\boldsymbol{c}} \tag{34}$$

Equation 33 can be rewritten as:

$$\left[\boldsymbol{K}_{\text{str}} - \lambda \boldsymbol{K}_{\text{aero}}^{\star}\right] \cdot \boldsymbol{q} = 0 \tag{35}$$

The matrix that multiplies the nodal displacement vector $\boldsymbol{q}$ takes the meaning of aeroelastic stiffness matrix and includes the structural stiffnesss matrix ($\boldsymbol{K}_{\text{str}}$) and the aerodynamic stiffness matrix ($-\lambda \boldsymbol{K}_{\text{aero}}^{\star}$). The latter depends on the free stream velocity because of the presence of the term λ (see Eq. 34).

The system is statically unstable (divergence) when the aeroelastic stiffness matrix becomes singular. In other words, when Eq. 33 is satisfied for non-zero nodal vector $\boldsymbol{q}$. This is a typical eigenvalue problem. The smallest real positive value λ_{min} is directly related to the divergence speed:

$$V_D = \sqrt{\frac{2\,\lambda_{\text{min}}}{\rho_\infty}} \tag{36}$$

7 Results and discussion

Several wing configurations with different geometries, layout and loadings are considered. Two different types of response solutions are investigated and compared in this work. The first one coincides with the static structural analysis, hereinafter referred as SSA, and involves only the structural stiffness matrix by disabling the aerodynamic matrix $\boldsymbol{K}_{\text{aero}}$. Hence, the following system is solved:

$$\boldsymbol{K}_{\text{str}} \cdot \boldsymbol{q} = \boldsymbol{L}_{\text{RHS}} \tag{37}$$

The second solution is the SAA which solves the aeroelastic system (Eq. 32) by adding the aerodynamic stiffness matrix to the elastic one.

Straight and swept wing configurations as well as rectangular and airfoil shaped cross-sections are considered. Unless otherwise specified, they are subjected to a pure aerodynamic loading (vector $\boldsymbol{L}_{\text{RHS}}$) and modeled with a one-dimensional mesh of 20 B4 elements along the y axis. This choice ensues from the conclusions made in previous CUF works on thick and thin-walled structures [39, 40]. Cantilever boundary condition on half-wings is imposed and the symmetry condition is exploited in the aerodynamic computation. Both isotropic and anisotropic composite materials are taken into account and a further analysis evaluates the combined effect of the material lamination and the sweep angle on the divergence speed of a composite wing.

In the following analyses, the wings are exposed to a free stream velocity $\boldsymbol{V}_\infty$ parallel to the x axis with an angle of attack α. The assessment of the vortex lattice formulation in computing $\boldsymbol{L}_{\text{RHS}}$ was carried out in [40]. A result is here retrieved in order to evaluate the aerodynamic pressure distribution along different wing configurations.

An aft-swept wing with $\Lambda = 45°$ and a forward-swept wing with $\Lambda = -45°$ with a constant chord $c = 1$ m are considered as untapered reference configurations [41]. The half wing span-to-chord ratio L/c is equal to 2 and the terms C_l and C_L are introduced as follows:

$$C_l(y) = \frac{L^{\star}(y)}{\frac{1}{2}\rho_\infty V_\infty^2 2e(y)c(y)} \qquad C_L = \frac{L_{\text{RHS}}^{\text{tot}}}{\frac{1}{2}\rho_\infty V_\infty^2 L\bar{c}} \tag{38}$$

$$L_{\text{RHS}}^{\text{tot}} = \sum_{i=1}^{N_{AP}} \left(\boldsymbol{L}\right)_i = \sum_{i=1}^{N_{AP}} \frac{1}{2}\rho_\infty V_\infty^2 \tan(\pi - \alpha) \left(\boldsymbol{I}^{\text{D}} \left[\boldsymbol{A}^{\text{D}}\right]^{-1} \boldsymbol{d}\right)_i \tag{39}$$

where $c(y)$ and $L^{\star}(y)$ are the chord and the lift force generated by the pressure acting on the panels with span-length $2e$ (y) placed at the y coordinate, respectively. $L_{\text{RHS}}^{\text{tot}}$ is the total lift force acting on the right half-wing and Eq. 39

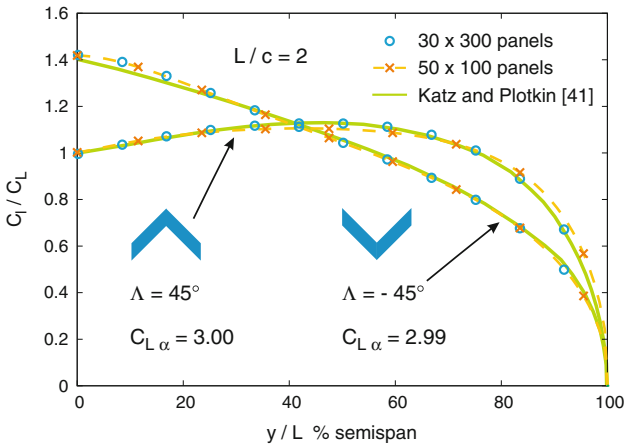

Fig. 3 Effect of the sweep angle on the spanwise loading for two reference untapered wings

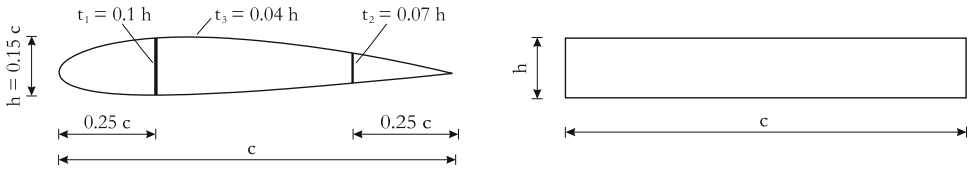

Fig. 4 Cross-sections used for the wing configurations

(a) NACA 2415 with 3 cells **(b)** Rectangular section

refers to Eq. 31. The air density is henceforth assumed to be $\rho_\infty = 1.225$ kg/m^3. The trend of the $\frac{C_l}{C_L}$ ratio along the y axis is shown for both the swept wings in Fig. 3. In the computation two different aerodynamic meshes are involved, differing in shape and in the total number of panels. It is interesting to note the influence of the sweep angle Λ on the pressure distribution and the position of the maximum pressure on the spanwise direction. A slight dependence on the aerodynamic mesh used is furthermore detected and notable mainly for the aft-swept case. An excellent agreement with the results obtained by Katz and Plotkin [41] is achieved.

For a straight configuration, it has been verified that the maximum pressure acts on the leading edge of each section, with an overall maximum placed on the root cross-section. The pressure distribution computed by the VLM decreases along the y axis according to the low-speed aerodynamics of aircraft straight wings [41]. It is noteworthy that the quantities α and V_∞ affect such a pressure distribution only in value, but not in shape.

7.1 Isotropic metallic wings

7.1.1 Airfoil-shaped wing

In this section, an isotropic aluminium with Young's modulus $E = 69$ GPa and Poisson's ratio $\nu = 0.33$ is introduced. A straight untapered wing is exposed to a free stream velocity $V_\infty = 50$ m/s with $\alpha = 3°$. The half-wing span L is equal to 5 m and the chord is $c = 1$ m. The cross-section adopted is a thin-walled NACA 2415 airfoil, which is subdivided into three cells by two spars along the spanwise direction inserted at 25 and 75 % of the chord, see Fig. 4a. The front and rear spars' thicknesses are, respectively, 10 and 7 % of the airfoil height, whereas the percentage is 4 % for the skin. The considered airfoil height-to-chord ratio is 0.15. An aerodynamic mesh composed of 4×40 panels is set on the reference surface of the structure.

A convergence study is carried out to evaluate the combined effect of the number of B4 finite elements N_{EL} and the expansion order N on the static aeroelastic response (SAA) of the wing. The mechanics of the structure is described in terms of the maximum transverse displacement $u_{z\max}$, which is located at the trailing edge of the tip cross-section. This location derives from the aeroelastic coupling between the twist and the vertical bending of the wing exposed to the free stream. The results for SAA are shown in Table 1.

Table 1 Convergence study: effect of the number of B4 elements on $u_{z\max}$ (mm) for different beam models

N_{EL}	EBBM	TBM	$N = 1$	$N = 1$[a]	$N = 2$	$N = 3$	$N = 4$
2	8.9407	8.9506	8.9603	6.0532	8.3904	8.4972	8.5134
5	8.9407	8.9506	8.9603	6.0532	8.5810	8.7112	8.7315
10	8.9407	8.9506	8.9603	6.0532	8.6393	8.7734	8.7953
20	8.9407	8.9506	8.9603	6.0532	8.6673	8.8015	8.8245
40	8.9407	8.9506	8.9603	6.0532	8.6800	8.8136	8.8377

Straight metallic airfoil-shaped wing. $V_\infty = 50$ m/s, $\alpha = 3°$, 4×40 panels. SAA

[a] Poisson's locking is not corrected

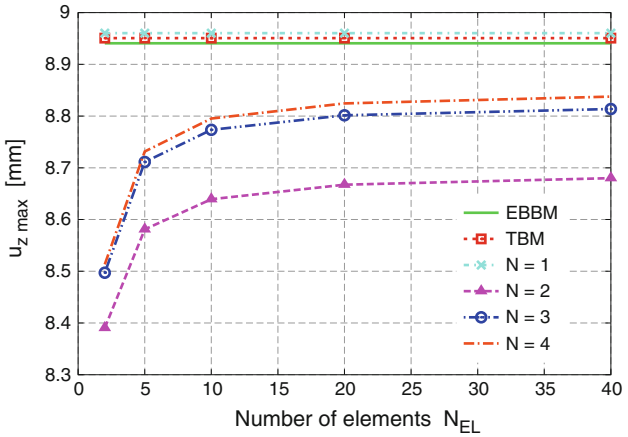

Fig. 5 Maximum transverse displacement $u_{z\ \max}$ as a function of the structural mesh and the models involved. Straight metallic airfoil-shaped wing. SAA

The numerical convergence on N_{EL} is achieved for each adopted theory as reported in Fig. 5. A higher number of elements enhances the flexibility of the structure with the exception of first-order theories EBBM, TBM, and $N = 1$, in which cases the results are slightly different and not affected by the mesh.

The maximum displacement increases with N for any mesh, to such an extent that no remarkable differences are detected for high-order expansion. It is interesting to note how $u_{z\max}$ decreases when the theory changes from a

first-order to a second-order form. The main reason for this turnaround stands in Poisson's locking correction adopted only for classical and first-order theories [46]. In fact, by disabling such a correction for $N = 1$, $u_{z\max}$ would be even lower than the second-order case, see Table 1. Thus, an approximation with an order higher than the first yields a more flexible structure.

The comparison of the aeroelastic response of the wing with MD NASTRAN, which is taken as reference shell model, is now faced. While the proposed CUF 1D model is able to easily handle arbitrary cross-section geometries for both SSA and SAA analyses, the choice of an airfoil-shaped wing requires an equivalent procedure in MD NASTRAN for the aeroelastic analysis (sol 144). The procedure here used involves an equivalent flat plate with a rectangular cross-section which is supposed to approximately emulate the bending and torsional behavior of the actual wing. This technique retrieves the results of structural response (SSA) for the same airfoil-shaped wing analyzed in [40] and summarized in Table 2. In that case, an equivalent procedure was not necessary because the MD NASTRAN structural analysis (sol 101) was carried out by charging the front skin of the airfoil-shaped wing (solid elements -10^6 DOFs) with the pressures due to the pure aerodynamic loading computed by the VLM (vector $\boldsymbol{L}_{\text{RHS}}$).

The equivalent height $h_{\text{eq}} = 80.382$ mm is now chosen so that the associated equivalent wing and the airfoil-shaped wing show the same value for $u_{z\max}$ computed by MD NASTRAN (SSA), see second and third columns of Table 2. Hence the aeroelastic analysis is carried out only on the equivalent flat plate via MD NASTRAN (sol 144) and the results are compared with the fourth-order model (SAA) in Table 3.

The results about the equivalent flat plate in Tables 2 and 3 show an excellent agreement of the 1D higher-order model with the reference solution (error of 0.029 % for SSA and 0.041 % for SAA). On the contrary, the comparison between the equivalent flat plate via MD NASTRAN and the actual airfoil shaped wing via $N = 4$ leads the error to be no more negligible, mainly for the aeroelastic response analysis (0.106 % for SSA vs. 1.480 % for SAA). Thus, the procedure used introduces a further relevant approximation

Table 2 Comparison of the structural response (SSA) of the airfoil-shaped wing and the equivalent flat plate between MD NASTRAN and $N = 4$ (40 B4 elements)

SSA	MD NASTRAN Airfoil wing	MD NASTRAN Flat plate	$N = 4$ Flat plate	$N = 4$ Airfoil wing
$u_{z\max}$	8.6762	8.6762	8.6787	8.6854
% Diff	–	+0.000 %	+0.029 %	+0.106 %
DOFs	10^6	1,845	5,445	5,445

Table 3 Comparison of the aeroelastic response (SAA) of the airfoil-shaped wing and the equivalent flat plate between MD NASTRAN and $N = 4$ (40 B4 elements)

SSA	MD NASTRAN Flat plate	$N = 4$ Flat plate	$N = 4$ Airfoil wing
$u_{z\max}$	8.7088	8.7124	8.8377
% Diff	–	+0.041 %	+1.480 %
DOFs	1,845	5,445	5,445

of the actual aeroelastic behavior of the structure. In fact, the in-plane deformation of the cross-section plays an important role as proved in [40], where the same NACA 2415 profile is considered. The present 1D model is able to handle even complex cross-section geometries also for the aeroelastic analysis without increasing the number of DOFs. This model does not require the introduction of an equivalent flat plate to study the structural and aeroelastic response of arbitrary wings via a low number of DOFs (5,445 vs. 10^6 for MD NASTRAN).

7.1.2 *Rectangular cross-section*

A thin rectangle is now taken into account as cross-section for the straight wing introduced above. Referring to Fig. 4b, the considered height-to-chord ratio is 0.02 (h = 20 mm). An aerodynamic mesh composed of 10 × 50 panels is set on the reference surface of the structure, which is exposed to an increasing free stream velocity with $\alpha = 1°$.

Table 4 reports a parametric study on the maximum transverse displacement, placed again at the leading edge of the tip cross-section, as the free stream velocity changes. The aeroelastic responses are evaluated. The values of $u_{z\max}$ would increase linearly with the square of V_∞ for SSA since $\boldsymbol{K}_{\text{str}}$ does not depend on V_∞ and the problem is linear. The same does not occur for SAA as the contribution of $\boldsymbol{K}_{\text{aero}}$ to the system stiffness becomes more evident as V_∞ increases. As a consequence, the difference from SSA gets more significant for $V_\infty = 50$ m/s. The accuracy of the aeroelastic analysis by the present CUF 1D model increases with the

Table 4 Effect of the free stream velocity V_∞ (m/s) on $u_{z\max}$ (mm)

Model	$V_\infty = 10$	$V_\infty = 30$	$V_\infty = 50$
EBBM	7.6272	68.611	190.40
TBM	7.6272	68.611	190.40
$N = 1$	7.6275	68.622	190.48
$N = 2$	7.0244	68.236	224.45
$N = 3$	7.4966	73.241	243.94
$N = 4$	7.5126	73.397	244.46
NASTRAN	7.5446	73.731	245.49

Straight wing, c = 1 m, L = 5 m, h = 20 mm. 20 B4 elements. $\alpha = 1°$, 10 × 50 panels. SAA

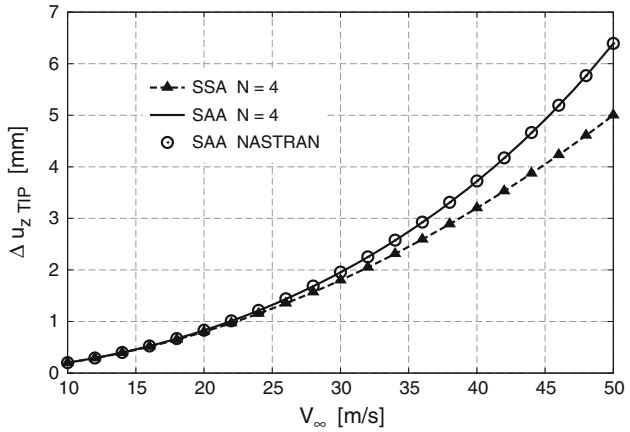

Fig. 6 Effect of V_∞ on the twist $\Delta u_{z\ \mathrm{TIP}}$. Isotropic material. SSA vs. SAA

expansion order N by approaching the reference shell results as reported in Table 4. It should be noticed that EBBM and TBM used here and in the following analyses are unable to handle any torsional behavior since no warping functions, e.g. in Vlasov beam model, have been implemented. However, $N = 1$ model takes into account torsional effects in the displacement field but it results to be ineffective especially when the aeroelastic effect on the wing is relevant.

The twist of the tip cross-section ($y = L$) for the structural and aeroelastic responses is investigated by means of the quantity Δu_z, which is defined as the difference of u_z between the leading and trailing edges. The simulation is performed via a fourth-order approximation and the results are shown in Fig. 6. It is interesting to note the raising importance of the aeroelastic effect of V_∞ on the tip section twist and the excellent agreement between MD NASTRAN (sol 144) and the higher-order model, which is able to properly describe the three-dimensional behavior of the structure unlike first-order beam theories.

A parametric study on the influence of the aspect ratio on the response of the straight wing is carried out and summarized in Table 5. The chord length is maintained constant and the half-wing span L ranges from 5 to 25 m whereas the thickness is $h = 100$ mm. Poisson's locking correction is not sufficient to make first-order approximation models effective in computing the maximum displacement for SSA, since the tip section twist and warping become relevant especially for slender wings. Moreover, the increasing aeroelastic effect with the aspect ratio is detectable only by means of a higher-order model, which accurately approaches the shell solution as L increases (SAA).

The dimensionless quantity $u^{\star}_{z\mathrm{TIP}}$ is introduced to study the bending behavior of the wing. It represents the transverse displacement at the midpoint of the tip cross-section normalized with respect to $\bar{u}_{z\mathrm{TIP}}$, which is the tip-maximum displacement of a cantilever beam subjected to a uniformly distributed load $q = L^{\mathrm{tot}}_{\mathrm{RHS}}/L$:

$$\bar{u}_{z\mathrm{TIP}} = \frac{qL^4}{8EI} \Rightarrow u^{\star}_{z\mathrm{TIP}} = \frac{u_{z\mathrm{TIP}}}{\bar{u}_{z\mathrm{TIP}}} = u_{z\mathrm{TIP}} \frac{8EI}{L^{\mathrm{tot}}_{\mathrm{RHS}} L^3} \tag{40}$$

The free stream velocity would have no effect on $\bar{u}_{z\mathrm{TIP}}$ for SSA. In fact, in this case the raising V_∞ would modify the aerodynamic pressure distribution only in value, but not in shape. In fact, $L^{\mathrm{tot}}_{\mathrm{RHS}}$ would increase linearly with the square of V_∞ as well as $u_{z\mathrm{TIP}}$. On the contrary, the span

Table 5 Effect of the length L (m) on $u_{z\mathrm{max}}$ (mm)

	$L = 5$		$L = 10$		$L = 20$	
	SSA	SAA	SSA	SAA	SSA	SAA
EBBM	2.9900	2.9899	56.353	56.347	1,000.24	999.56
	−0.0024 %[a]		−0.0114 %		−0.0679 %	
TBM	2.9911	2.9910	56.358	56.352	1,000.25	999.57
	−0.0024 %		−0.0115 %		−0.0677 %	
$N = 1$	2.9928	2.9933	56.366	56.402	1,000.28	1,002.99
	+0.0137 %		+0.0647 %		+0.2705 %	
$N = 2$	2.8620	2.8731	54.631	55.717	981.43	1,075.78
	+0.3863 %		+1.9864 %		+9.6135 %	
$N = 3$	2.9192	2.9307	55.358	56.465	988.76	1,084.07
	+0.3945 %		+2.0004 %		+9.6387 %	
$N = 4$	2.9325	2.9443	55.478	56.611	989.72	1,087.30
	+0.4020 %		+2.0419 %		+9.8598 %	
NASTRAN	–	2.9505	–	56.723	–	1,092.77

20 B4 elements. Straight wing, chord = 1 m, h = 100 mm. 20 B4 elements. $V_\infty = 70$ m/s, $\alpha = 1°$, 10×50 panels. SSA vs. SAA

[a] Difference between SAA and SSA

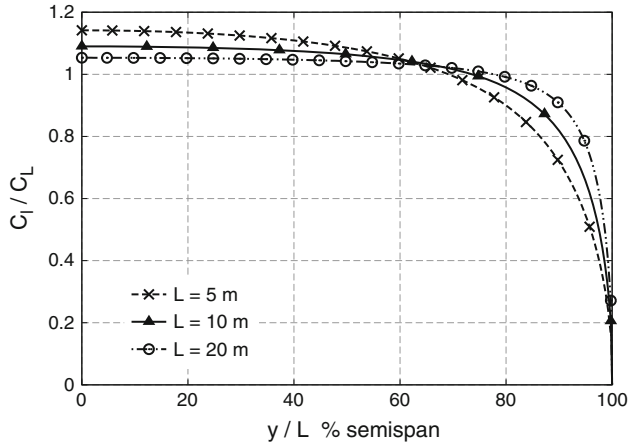

Fig. 7 Effect of L on the spanwise aerodynamic loading. Straight wing. Isotropic material. SSA vs. SAA

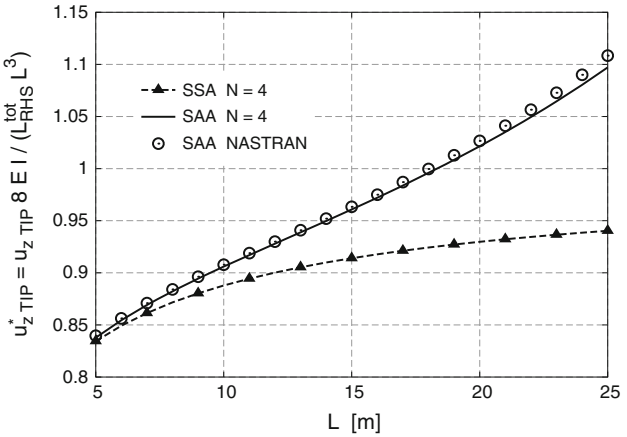

Fig. 8 Effect of L on the dimensionless $u^{\star}_{z\mathrm{TIP}}$. Isotropic material. SSA vs. SAA

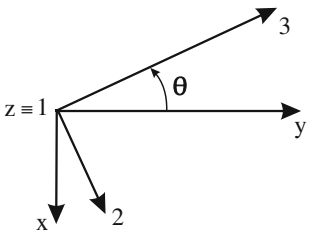

Fig. 9 Definition of the fiber orientation angle

parameter modifies the distribution of aerodynamic pressures acting on the reference surface exposed to the free stream (vector $\boldsymbol{L}_{\mathrm{RHS}}$) not only in value, but also in shape. Figure 7 emphasizes the role played by the aspect ratio on this aerodynamic pressure, whose trend approaches a uniformly distributed load as L increases. The progress of the dimensionless quantity $u^{\star}_{z\mathrm{TIP}}$ is thus no more a constant straight line for SSA analysis, but rather a curve approaching the unit value, see Fig. 8. As far as the

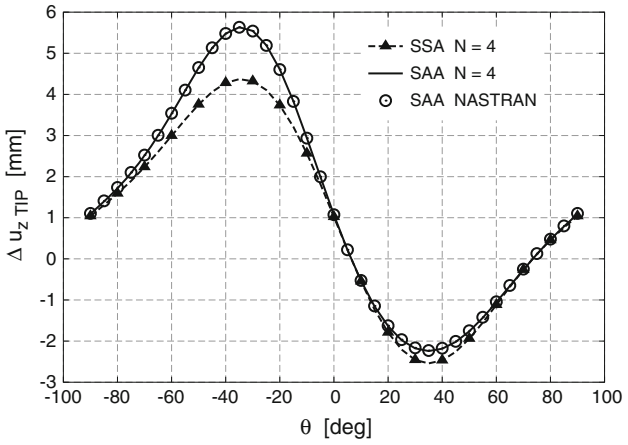

Fig. 10 Effect of the lamination on the torsion of the tip cross-section. Straight wing. Composite material. SSA vs. SAA

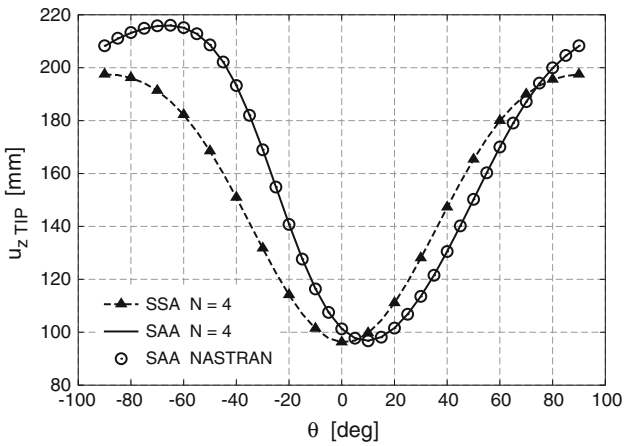

Fig. 11 Effect of the lamination on the bending of the tip cross-section (at the midpoint). Straight wing. Composite material. SSA vs. SAA

aeroelastic response is concerned, the influence of high aspect ratio on $u^{\star}_{z\mathrm{TIP}}$ depicted by the proposed 1D refined method ($N = 4$) is once more consistent with the shell results.

7.2 Anisotropic composite wings

A composite material is introduced to analyze the aeroelastic tailoring on a straight wing with length $L = 10$ m and chord $c = 1$ m. A compact rectangular cross-section with height $h = 100$ mm is considered. The material fibers are oriented along the longitudinal axis 3 with a lamination angle θ as shown in Fig. 9. Young's modulus along the longitudinal axis E_L is equal to 20.5 GPa, whereas those along the transverse directions 1 and 2 are equal to 10 GPa. Poisson's ratio and the shear modulus are the same in all directions. Indeed, $\nu_{12} = \nu_{13} = \nu_{23} = \nu = 0.25$ and $G_{12} = G_{13} = G_{23} = G = 5$ GPa. Figures 10 and 11 show

the influence of the lamination θ on the twist Δu_z and on the bending of the tip cross-section via $N = 4$ model. The bending is described via the transverse displacement of the midpoint placed at the tip section $u_{z\text{TIP}}$.

The comparison of SSA and SAA underlines the importance of the contribution of $\boldsymbol{K}_{\text{aero}}$ to evaluate the aeroelastic behavior of composite wings. While the curve of twist related to SSA is essentially anti-symmetric with respect to the $\theta = 0°$ lamination, the aeroelastic analysis shows a trend which is far from symmetric, see Fig. 10. In general, the aeroelastic analysis leads the twist of the unswept wing to be higher compared to the structural solution as the lamination changes, especially for negative values of θ. The same result occurs for bending behavior as shown in Fig. 11, where only the SSA case obtains an almost symmetric curve. However, the laminations which lead to the minimum and maximum twist conditions are the same for the structural and aeroelastic analyses, whereas they are different for the bending deflection.

The curves describing the tip twist as θ changes present some particular intersection points in which Δu_z reaches the same value for SSA and SAA. In general, these orientations differ from those which lead the tip bending to be the same for the structural and aeroelastic analyses. These lamination values depend on the wing geometry, the material properties and the aerodynamic conditions.

The numerical results summarized in Tables 6 and 7 reveal the role played by θ for different structural theories. The use of a composite material leads to move the maximum transverse displacement from the leading to the trailing edge for particular positive laminations (negative twist) unlike the isotropic case. The excellent agreement between the fourth-order beam model and MD NASTRAN-shell (sol 144) in describing the aeroelastic response of anisotropic wings with generic orientation is again noteworthy, whereas the diminishing expansion order N corresponds to a lower number of DOFs as well as loss of accuracy.

The aeroelastic response of the straight wing previously analyzed is carried out when a concentrated load applied at the tip cross-section is combined to the aerodynamic pressures. A mesh of 10 $B4$ elements and a higher-order model are involved ($N = 4$). Due to the material anisotropy, the tip transverse force P_z has an additional torsional effect along the span-wise direction which could be clockwise or counter-clockwise depending on the lamination angle's sign. As a consequence, the three-dimensional deflection of the wing is strongly affected by θ as depicted in Fig. 12 with a large scale factor.

The effect of tailoring on the divergence speed of a swept-forward wing structure is displayed in Fig. 13. Given a lamination, the lower is the sweep angle the lower is the divergence speed. In general, it is confirmed that for a forward-swept wing the divergence instability constitutes a more critical case with respect to an unswept one, due to the wash-in effect. However, for positive lamination angles V_{D} is so high that this critical phenomenon becomes negligible.

The lamination angle $\theta_{V_{\text{Dmin}}}$ associated to the minimum divergence speed depends on the sweep angle of the wing as well as the wing geometry. For the straight wing $\theta_{V_{\text{Dmin}}}$ is the value associated to the maximum tip twist of the aeroelastic response as depicted in Fig. 10. It highlights that the correct evaluation of the torsional and warping behavior of a structure is a mandatory issue for the model involved in the aeroelastic analysis.

Thus bending-torsion beam theories are appropriate to detect the wing divergence instability, unlike classical bending theories (EBBM and TBM). However, classical bending-torsion beam theories take into account torsion but let the beam cross-section to only rigidly rotate. Instead, the present models take into account the three-dimensional deformation of each single point of the structure with an increasing accuracy as N increases, see Eq. 7. Thus it becomes difficult to define what torsion really is for refined models able to detect a three-dimensional displacement field in lieu of a simplified rigid torsion field. Especially for

Table 6 Effect of the lamination on the twist $\Delta u_{z\text{TIP}}$ (mm) of the tip cross-section

θ	SSA $N = 4$	SAA $N = 2$	SAA $N = 3$	SAA $N = 4$	SAA NASTRAN
−60°	2.9918	3.6114 (+2.00 %)	3.5076	3.5272 (−0.38 %)	3.5407
−30°	4.3163	5.5766 (+0.65 %)	5.5127	5.5395 (−0.02 %)	5.5408
0°	1.0206	1.0445 (−2.76 %)	1.0458	1.0704 (−0.34 %)	1.0741
30°	−2.4563	−2.2294 (+3.03 %)	−2.1959	−2.1741 (−0.48 %)	−2.1638
60°	−1.1191	−1.1574 (+10.9 %)	−1.0845	−1.0569 (+1.25 %)	−1.0439
90°	1.0390	1.0643 (−3.81 %)	1.0656	1.0909 (−1.41 %)	1.1065
DOFs	1,395	558	930	1,395	2,135

Straight wing, c = 1 m, L = 10 m, h = 100 mm. 10 B4 elements. $V_\infty = 50\,\text{m/s}$, $\alpha = 1°$, 10×50 panels. Composite material. SSA vs. SAA

Table 7 Effect of the lamination on the bending of the wing: $u_{z\text{TIP}}$ (mm) at the midpoint of the tip cross-section

θ	SSA $N = 4$	SAA $N = 2$	SAA $N = 3$	SAA $N = 4$	SAA NASTRAN
$-60°$	181.956	214.518 (-0.31 %)	214.494	214.826 (-0.16 %)	215.175
$-30°$	131.597	168.142 (-0.49 %)	168.557	168.898 (-0.04 %)	168.965
$0°$	96.152	100.656 (-0.62 %)	101.071	101.246 (-0.04 %)	101.288
$30°$	127.888	112.284 (-1.12 %)	113.212	113.488 (-0.06 %)	113.555
$60°$	179.707	167.586 (-1.42 %)	169.346	169.753 (-0.15 %)	170.007
$90°$	197.216	206.892 (-0.67 %)	207.548	207.869 (-0.21 %)	208.297
DOFs	1,395	558	930	1,395	2,135

Straight wing, c = 1 m, L = 10 m, h = 100 mm. 10 B4 elements. $V_\infty = 50\,\text{m/s}$, $\alpha = 1°$, 10×50 panels. Composite material. SSA vs. SAA

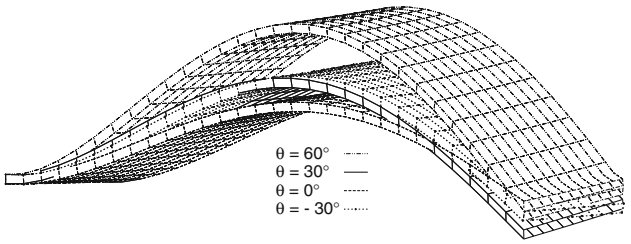

Fig. 12 3D deformation of the straight composite wing. Aeroelastic response with tip transverse force $P_z = -515.5$ N. V_∞ = 50 m/s, $\alpha = 1°$

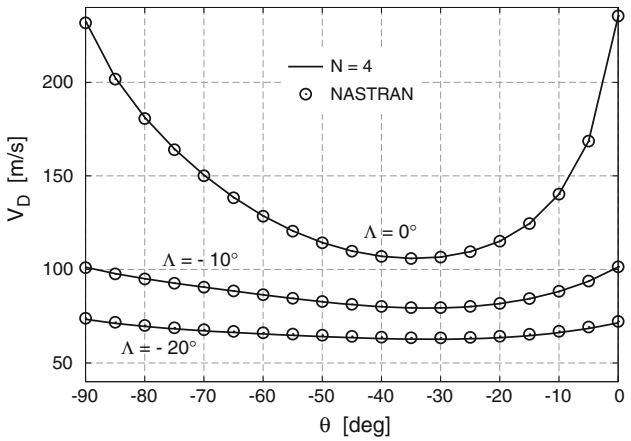

Fig. 13 Combined effects of the lamination θ and the sweep angle Λ on the divergence speed V_D. Composite material

aeroelastic analysis of thin-walled wings, this model capability could play a crucial role since the aerodynamic field is significantly affected by the cross-section warping and in-plane deformations. The capabilities of the present higher-order models are proved in comparison with FE shell results, see Table 8. It should be remarked that the refined CUF 1D model requires a limited number of DOFs to detect the wing divergence speed with an error no higher than 0.5 % with respect to the reference shell solution. Although a simple section geometry has been used here for a direct comparison with MD NASTRAN, the number of

Table 8 Effect of the lamination on the divergence speed V_D (m/s)

θ	$N = 4$	NASTRAN	% Diff
$-90°$	232.8142	231.7779	+0.4471
$-75°$	164.5029	163.9645	+0.3284
$-60°$	128.6913	128.4517	+0.1865
$-45°$	109.8690	109.7624	+0.0971
$-30°$	106.6362	106.5942	+0.0394
$-15°$	124.5134	124.5123	+0.0009
$0°$	235.1681	235.4656	-0.1263
DOFs	1,395	2,135	-34.66

Straight wing, c = 1 m, L = 10 m, h = 100 mm. 10 B4 elements. $\alpha = 1°$, 10×50 panels. Composite material

DOFs necessary to the present model would be remarkably lower especially for complex section geometries.

8 Conclusions

This paper has proposed the aeroelastic model that couples the VLM and a refined one-dimensional structural model with in-plane warping and plate/shell capabilities. The model has been assessed in excellent agreement with available results from the literature as well as MD NASTRAN software. Classical beam theories such as Euler–Bernoulli and Timoshenko have been obtained as particular cases. Therefore, this has made the comparison with higher-order models to be easily achieved for the structural and aeroelastic response as well as the divergence instability identification. Moreover, the CUF model has been able to detect in which case the first-order beam theories are accurate enough to describe the structural behavior of a beam-like system and in which case the use of refined theories is mandatory. In general, the model here formulated can handle arbitrary cross-section geometries for moderate and high aspect ratio beam-like structures, with no limitations on the composite lamination properties. However, for multilayered cross-sections an expansion of Lagrange polynomials for CUF and a layerwise approach may be preferred to

detect local effects of composite materials. Both the static structural and aeroelastic analyses can be performed with a limitated number of DOFs in a good agreement with commercial software. Future works will investigate even more the method's capabilities especially in case of complex cross-section layouts and unconventional wing configurations. The choice of the cross-section geometrical shape will not affect the number of DOFs of the present model, unlike shell and solid finite elements codes.

References

1. Patil, M.J., Hodges, D.H., Cesnik, C.E.S.: Nonlinear aeroelasticity and flight dynamics of high-altitude long-endurance aircraft. J. Aircraft **38**(1), 88–94 (2001)
2. Sulaeman, E., Kapania, R.K., Haftka, R.T.: Parametric studies of flutter speed in a strut-braced wing. In: 43rd AIAA/ASME/ASCE/AHS/ASC Structures, Structural Dynamics, and Materials Conference, AIAA Paper 2002-1487, Denver (2002)
3. Bhatia, M., Kapania, R.K., Van Hoek, M., Haftka, R.T.: Structural design of a truss braced wing: potential and challenges. In: 50th AIAA/ASME/ASCE/AHS/ASC Structures, Structural Dynamics, and Materials Conference, AIAA Paper 2009-2147, Palm Springs (2009)
4. Demasi, L., Livne, E.: Aeroelastic coupling of geometrically nonlinear structures and linear unsteady aerodynamics: two formulations. J. Fluids Struct. **25**(5), 918–935 (2009)
5. Demasi, L., Livne, E.: Dynamic aeroelasticity of structural nonlinear configurations using linear modally reduced aerodynamic generalized forces. AIAA J. **47**(1), 71–90 (2009)
6. Pamadi, B. N.: Performance, Stability, Dynamics, and Control of Airplanes, 2nd edn. AIAA, Maryland (2004)
7. Shirk, M.H., Hertz, T.J., Weisshaar, T.A.: Aeroelastic tailoring—theory, practice, and promise. J. Aircraft **23**(1), 6–18 (1986)
8. Weisshaar, T.A.: Divergence of forward swept composite wings. J. Aircraft **17**(6), 442–448 (1980)
9. Weisshaar, T.A.: Aeroelastic tailoring of forward swept composite wings. J. Aircraft **18**(8), 669–676 (1981)
10. Weisshaar, T.A.: Aeroelastic tailoring—creative uses of unusual materials. In: 28th Structures, Structural Dynamics, and Materials Conference, AIAA-87-0976-CP, Monterey (1987)
11. Housner, J.M., Stein, M.: Flutter analysis of swept-wing subsonic aircraft with parametric studies of composite wings. Technical report, Sept. NASA-TN-D-7539 (1974)
12. Librescu, L., Song, O.: On the static aeroelastic tailoring of composite aircraft swept wings modelled as thin-walled beam structures. Compos. Eng. **2**(5–7), 497–512 (1992)
13. Patil, M.J.: Aeroelastic tailoring of composite box beams. In: 35th Aerospace Sciences Meeting and Exhibit, AIAA Paper 97-0015, Reno (1997)
14. Qin, Z., Librescu, L.: Aeroelastic instability of aircraft wings modelled as anisotropic composite thin-walled beams in incompressible flow. J. Fluids Struct. **18**(1), 43–61 (2003)
15. Jeon, S.M., Cho, M.H., Lee, I.: Aeroelastic analysis of composite rotor blades in hover. Comput. Struct. **66**(1), 59–67 (1998)
16. Jeon, S.M., Lee, I.: Aeroelastic response and stability analysis of composite rotor blades in forward flight. Compos. Part B **32**(3), 249–257 (2001)
17. Kameyama, M., Fukunaga, H.: Optimum design of composite plate wings for aeroelastic characteristics using lamination parameters. Comput. Struct. **85**(3–4), 213–224 (2007)
18. Librescu, L., Maalawi, K.Y.: Aeroelastic design optimization of thin-walled subsonic wings against divergence. Thin Walled Struct. **47**(1), 89–97 (2009)
19. Kapania, K., Raciti, S.: Recent advances in analysis of laminated beams and plates, part I: shear effects and buckling. AIAA J. **27**(7), 923–934 (1989)
20. Kapania, K., Raciti, S.: Recent advances in analysis of laminated beams and plates, part II: vibrations and wave propagation. AIAA J. **27**(7), 935–946 (1989)
21. Kim, C., White, S.R.: Thick-walled composite beam theory including 3-D elastic effects and torsional warping. Int. J. Solid Struct. **34**(31–32), 4237–4259 (1997)
22. Carrera, E., Petrolo, M., Zappino, E.: Performance of CUF approach to analyze the structural behavior of slender bodies. J. Struct. Eng. **138**(2), 285–297 (2012)
23. Euler, L.: De Curvis Elasticis. Bousquet, Lausanne and Geneva (1744)
24. Timoshenko, S.P., Goodier, J.N.: Theory of Elasticity. McGraw-Hill, New York (1970)
25. El Fatmi, R.: Non-uniform warping including the effects of torsion and shear forces. Part I: a general beam theory. Int. J. Solids Struct. **44**(18–19), 5912–5929 (2007)
26. El Fatmi, R.: Non-uniform warping including the effects of torsion and shear forces. Part II: analytical and numerical applications. Int. J. Solids Struct. **44**(18–19), 5930–5952 (2007)
27. Schardt, R.: Eine erweiterung der technischen biegetheorie zur berechnung prismatischer faltwerke. Der Stahlbau **35**, 161–171 (1966)
28. Silvestre, N., Camotim, D.: First-order generalised beam theory for arbitrary orthotropic materials. Thin Walled Struct. **40**(9), 755–789 (2002)
29. Silvestre, N., Camotim, D.: Second-order generalised beam theory for arbitrary orthotropic materials. Thin Walled Struct. **40**(9), 791–820 (2002)
30. Berdichevsky, V., Armanios, E., Badir, A.: Theory of anisotropic thin-walled closed-cross-section beams. Compos. Eng. **2**(5–7), 411–432 (1992)
31. Volovoi, V.V., Hodges, D.H.: Theory of anisotropic thin-walled beams. J. Appl. Mech. **67**(3), 453–459 (2000)
32. Popescu, B., Hodges, D.H.: On asymptotically correct Timoshenko-like anisotropic beam theory. Int. J. Solids Struct. **37**, 535–558 (2000)
33. Yu, W., Volovoi, V.V., Hodges, D.H., Hong, X.: Validation of the variational asymptotic beam sectional analysis (VABS). AIAA J. **40**(10), 2105–2113 (2002)
34. Yu, W., Hodges, D.H.: Generalized Timoshenko theory of the variational asymptotic beam sectional analysis. J. Am. Helicopter Soc. **50**(1), 46–55 (2005)
35. Carrera, E.: Theories and finite elements for multilayered plates and shells: a unified compact formulation with numerical assessment and benchmarking. Arch. Comput. Methods Eng. **10**(3), 215–296 (2003)
36. Carrera, E., Giunta, G., Petrolo, M.: Beam Structures: Classical and Advanced Theories. Wiley, New York (2011)
37. Carrera, E., Giunta, G.: Refined beam theories based on a unified formulation. Int. J. Appl. Mech. **2**(1), 117–143 (2010)
38. Carrera, E., Petrolo, M., Varello, A.: Advanced beam formulations for free vibration analysis of conventional and joined wings. J. Aerospace Eng. **25**(2), 282–293 (2012)
39. Carrera, E., Petrolo, M.: On the effectiveness of higher-order terms in refined beam theories. J. Appl. Mech. **78**(2), 021013.1–021013.17 (2010)
40. Varello, A., Carrera, E., Demasi, L.: Vortex lattice method coupled with advanced one-dimensional structural models. J. Aeroelasticity Struct. Dyn. **2**(2), 53–78 (2011)

41. Katz, J., Plotkin, A.: Low-Speed Aerodynamics. Cambridge University Press, Cambridge (2001)
42. Harder, R., Desmarais, R.N.: Interpolation using surface splines. J. Aircraft **9**(2), 189–191 (1972)
43. Harder, R., MacNeal, R., Rodden, W.: A design for the incorporation of aeroelastic capability into Nastran. NASA report, N71-33303 (1977)
44. Varello, A., Demasi, L., Carrera, E., Giunta, G.: An improved beam formulation for aeroelastic applications. In: 51st AIAA/ASME/ASCE/AHS/ASC Structures, Structural Dynamics, and Materials Conference, AIAA Paper 2010-3032, Orlando (2010)
45. Jones, R.: Mechanics of Composite Materials. 2nd edn. Taylor & Francis, Philadelphia (1999)
46. Carrera, E., Brischetto, S.: Analysis of thickness locking in classical, refined and mixed multilayered plate theories. Compos. Struct. **82**(4), 549–562 (2008)
47. Bathe, K.J.: Finite Element Procedures. Prentice Hall, Upper Saddle River, New Jersey (1996)
48. Carrera, E., Petrolo, M.: Refined one-dimensional formulations for laminated structure analysis. AIAA J. **50**(1), 176–189 (2012)